ADVANCED BIOLOGY
www.advanced-bio.com

3D Bioelectronic Model of the Human Intestine

*Chrysanthi-Maria Moysidou, Charalampos Pitsalidis, Mohammed Al-Sharabi, Aimee M. Withers, J. Axel Zeitler, and Róisín M. Owens**

Organ on chip (OoC) technologies have the potential to improve the translation of promising therapies currently failing in clinical trials at great expense and time due to dissimilarities between animal and human biology. Successful OoC models integrate human cells within 3D tissues with surrounding biomolecular components, and have benefited from the use of inert 3D gels and scaffolds used as templates, prompting tissue formation. However, monitoring technologies used to assess tissue integrity and drug effects are ill adapted to 3D biology. Here, a tubular electroactive scaffold serves as a template for a 3D human intestine, and enables dynamic electrical monitoring of tissue formation over 1 month. Cell- and extracellular matrix component-invoked changes in the properties of the scaffold alleviate the need for posthoc placement of invasive metallic electrodes or downstream analyses. Formation of in vivo-like stratified and polarized intestinal tissue compete with lumen contrasts with other quasi-3D models of the intestine using rigid porous membrane to separate cell types. These results provide unprecedented real-time information on tissue formation with highly sensitive multimodal operation, thanks to dual electrode and transistor operation. This device and the methodology for tissue growth within it represents a paradigm shift for disease modeling and drug discovery.

1. Introduction

The intestinal epithelium constitutes the largest and most essential barrier of the human body against the external environment,[1] acting as a dynamic and functional permeable barrier effectively blocking the passage of potential pathogens and toxins as well as hosting commensal microbes and their metabolites,[1,2] now known to play a central role in human health and disease.[3] It is additionally responsible for the absorption of dietary nutrients, solutes and ions from the gut lumen into the vasculature and regulation of drug metabolism.[1,2,4] Rodents remain the most commonly used animal model for studies of intestinal pathophysiology.[5–7] However, dissimilarities between animal and human biology have resulted in promising pre-clinical therapies failing to achieve translation at great cost of time and money.[8] In vitro models that recapitulate the complexity and functions of the human intestine can bridge the gap, generating more physiologically relevant data of human intestinal (patho-)physiology and uncovering potential therapeutic treatments.[4,9,10]

Until recently, such efforts have been limited to 2D models, which rely on culturing established human intestinal cell lines within Transwell insert culture setups, where they form polarized epithelial monolayers.[4,11] The reductionist nature of the 2D environment is however an inaccurate representation of the complex intestinal cell and tissue morphology, overlooking important biological parameters that influence the physiology of cellular networks and tissues as well as cell–cell and cell–matrix interactions, limiting the potential to form more complex tissue-like structures.[10,12,13] More sophisticated, 3D models that facilitate dynamic interactions between multiple cell types, closely emulating the in vivo milieu, have thus been called for to provide a more reliable tool for evaluating drug safety and efficacy in humans, early in the drug development process.[9,10,14] Intestinal organoids are a promising alternative, proven to recapitulate the 3D intestinal architecture.[4,9,10,15] However, challenges include lack of access to the luminal side of the organoid and communication with other cell and tissue types, limiting their use for disease modeling and pharmacokinetic studies.[4,10]

Organ on chip (OoC) technologies may provide a compromise between biomimicry and ease of manipulation. Advances in microfabrication and microengineering have facilitated the development of sophisticated fluidic-based systems with continuously perfused chambers inhabited by living cells, giving precise control over delivery of nutrients and spatiotemporal tuning of oxygen and pH gradients.[10,16–19] Multi-organ microsystems, first shown by Shuler et al.[20] as well as "body-on-a-chip" systems, are also eminently feasible, as recently exemplified by a fluidically coupled vascularized multi-organ-chip-based system to study human pharmacokinetic responses.[21] OoC technologies are also increasingly going beyond 2D, focusing on generation of 3D tissues and integrating surrounding biomolecular components, benefitting from the use of gels and scaffolds acting as templates for 3D tissue formation.[22–24] Monitoring technologies used to assess tissue integrity and

C.-M. Moysidou, Dr. C. Pitsalidis, M. Al-Sharabi, A. M. Withers, Prof. J. A. Zeitler, Prof. R. M. Owens
Department of Chemical Engineering and Biotechnology
University of Cambridge
Philippa Fawcett Drive, Cambridge CB3 0AS, UK
E-mail: rmo37@cam.ac.uk

The ORCID identification number(s) for the author(s) of this article can be found under https://doi.org/10.1002/adbi.202000306.

DOI: 10.1002/adbi.202000306

drug effects are however, still predominantly based on 2D cultures of cells, ill-adapted to 3D biology. Ideally, the coupling of in-line sensors with OoC platforms should provide a non-invasive, real-time evaluation of cellular functionality, without compromising the ability to carry out end-point assays.[12,19] Disappointingly, although OoC is compatible with downstream analysis of effluents coupled with "omics" analyses,[25–27] most current approaches rely heavily on end-point assays such as histology, fluorescence microscopy and permeability assays, despite inherent limitations (e.g., artifacts introduced by the use of probes/tags/tracer molecules). In contrast, electrical transducers have been shown to provide a wealth of real-time information through non-invasive transduction of biological signals.[28–30]

Electrochemical impedance spectroscopy (EIS) is a well-established and reliable tool for directly and rapidly monitoring cells in situ (measuring adhesion, proliferation, and differentiation) demonstrated for drug toxicology and host–pathogen interaction studies.[18,28,31,32] EIS measurements are acquired by sweeping the frequency of an applied AC voltage while recording the amplitude and phase of the resulting AC current. EIS is routinely used to obtain Trans-epi/endo-thelial electrical resistance values, a commonly used parameter to quantitatively characterize the function and integrity of barrier tissues, such as the intestinal epithelium, with fast, non-invasive measurements.[33] Currently, this is done in settings where epithelial monolayers grow on porous membranes made of PDMS or plastic (e.g., Transwells).[28,31,32] Although a growing number of OoC applications integrate electrodes for real-time monitoring of barrier integrity,[18,34] most are designed for planar cultures of cells and are thus ill-adapted for monitoring complex 3D cultures. Some recent studies have focused on interfacing 3D biological models with electrical transducers, however integration has been limited to flat electrodes.[29,35–37] Traditional 2D metal electrodes used in these systems are rigid and have limited contact with the 3D tissues, resulting in a lack of intimate electrode-cell coupling necessary to accurately record a signal. In addition, increased fluidic resistance is a significant challenge for in-line 3D cell monitoring tools.[33,38]

Conducting polymer (CP) scaffolds made from poly(3,4-ethylenedioxythiophene) doped with poly(styrene sulfonate) (PEDOT:PSS) have the potential for more seamless integration with 3D cell cultures, while allowing the intimate cell-electrode coupling required for accurate signal transduction. These emerging smart materials have shown remarkable performance as tissue engineering substrates for hosting a variety of different cell and tissue types.[39–41] In addition to providing a 3D template for cell growth, the CP scaffold can also be effectively used to monitor cell growth and tissue formation, compatible with OoC designs and 3D cell biology.[33,42,43] We previously developed tubular 3D macroporous electroactive scaffolds for real-time monitoring of cell integrity and activity. We fine-tuned the electrical, mechanical, and biochemical properties of the scaffolds and showed proof of principle for continuous electrical monitoring of a simple 3D culture of mammalian cells over a period of 4 days, with our "tubistor" device, distinguishing between cell adhesion and barrier tissue formation.[44]

Here, we report a new generation of this tool, adapted to accommodate a 3D tissue model of the human intestine. We designed a new device structure, based on a hollow tube, to mimic the luminal architecture of the human gastrointestinal (GI) tract. The new version of the device effectively supports maintenance and monitoring of the human gut epithelium model with remarkable stability, for an extended period of 26 days. We reconstructed the intestinal tissue microenvironment using a human tri-culture cell model, resulting in a stratified, polarized epithelium lining the scaffold lumen, anchored on a lamina propria-like tissue layer. Bi-modal operation of the device, both as an electrode and as a transistor, provided high-content, comprehensive electrical readouts, non-invasively revealing valuable information on cell activity and tissue formation on the scaffolds in real time.

2. Design and Fabrication of the Bioelectronic Host-Platform of the 3D Human Intestine Model

For the luminal tubistor device (L-Tubistor) (**Figure 1**A), we fabricated porous CP scaffolds within T-shaped tubes, incorporating a hollow channel in the center of the scaffold, representing the gut lumen. The devices were mounted on well-plates (Figure 1B), maintaining a sterile environment for cell growth and monitoring (Figure S1, Supporting Information, shows the detailed stepwise fabrication process). The resulting 3D luminal structures exhibit an extensive network of interconnected mesoporous structure as shown by scanning electron microscopy (Figure 1C,D) and X-ray microcomputed tomography (XμCT) (Figure 1E,F and Movie S1, Supporting Information). 2D projection images were reconstructed to obtain 2D cross-sections of the sample at different locations (Figure S2, Supporting Information) as well as 3D renderings of the porous structures. The reconstructed XμCT images allowed calculation of the porosity of the bulk compartment of the L-Tubistor scaffolds at 76%. The configuration of the L-Tubistor enables bimodal operation of the device both as an electrode and as a transistor. In electrode-mode, frequency-dependent electrical measurements (EIS) may be carried out, with subsequent extraction of the relative resistance and capacitance changes by fitting the data to an equivalent circuit model. For EIS measurements the L-Tubistor is operated in a 2-electrode configuration where the 3D scaffold serves as the working electrode (WE) through an embedded single point base Au electrode and a platinum mesh, placed in close proximity to the WE inside the plastic housing, acts as the counter electrode (CE) (Figure 1G,H). Transistor-based measurements provide an additional, faster (and simpler) way to qualitatively assess tissue formation by measurement of device transconductance. The operation of the L-Tubistor is the same as in typical planar OECTs, despite the larger PEDOT:PSS channel. Application of positive gate bias induces penetration of cations from the electrolyte into the channel, compensating for anions and hole extraction, resulting in dedoping of PEDOT:PSS and decreasing the drain current, described by depletion mode of operation. High transconductance values, indicative of the volumetric capacitance, were expected due to the large size of the channels (Figure 1I,J). Indeed, the L-Tubistor actually exhibits improved output and transfer curves compared with our previous work.[44] The enhanced performance characteristics can be attributed

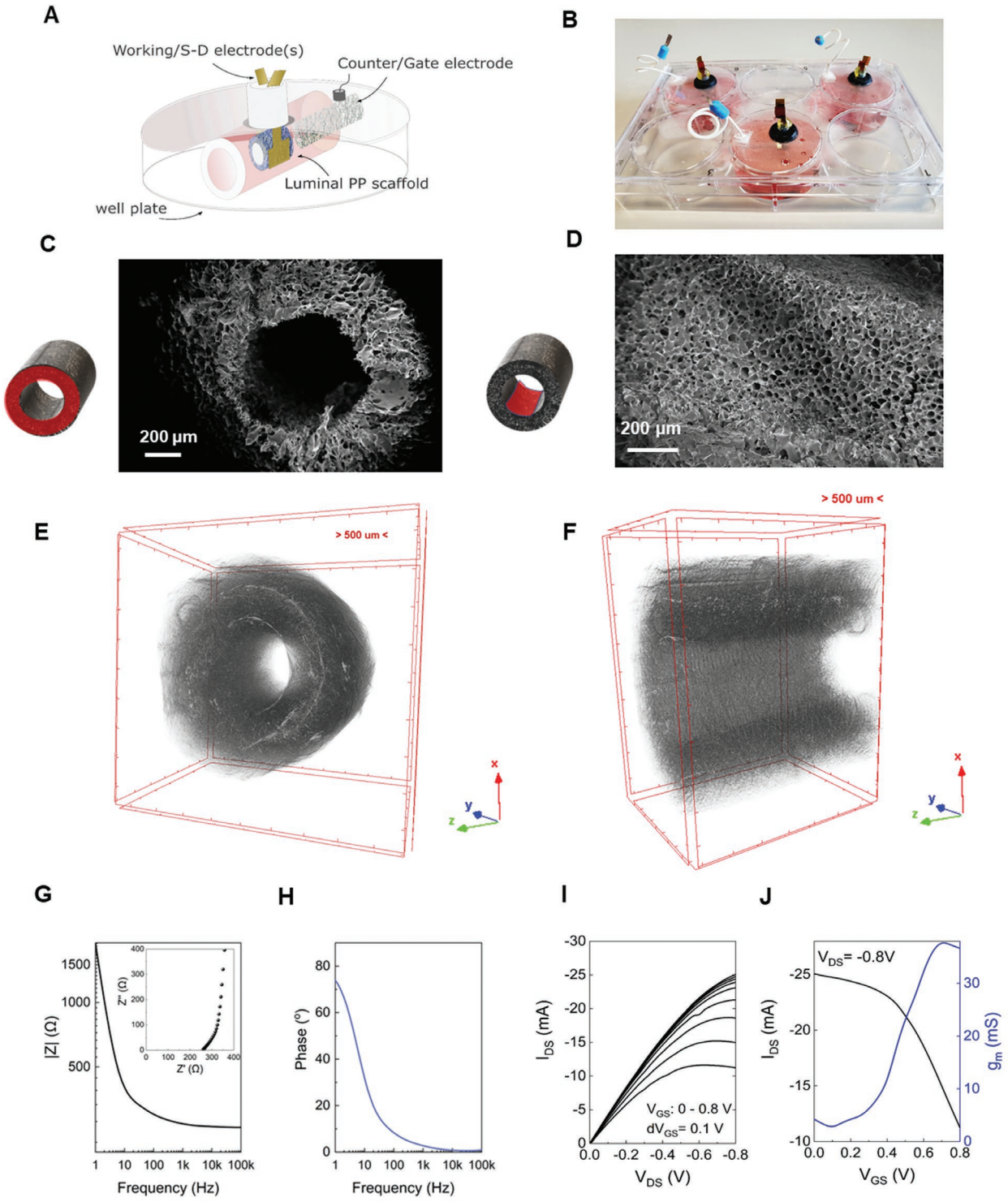

Figure 1. Device structure, optical and electrical characterization of the 3D bioelectronic human intestine platform. A) Schematic illustration of the bimodal (electrode/transistor) bioelectronic device used in this work. B) Photograph of the well-plate assembly, incorporating the tubular device constructs. The devices are mounted in a six well-plate using a push-fit connection (seen in black), keeping the electrical terminals outside each well (white wires). SEM images showing C) the transverse and D) the longitudinal section of the luminal PEDOT:PSS scaffolds. 3D visualization of the XµCT data of the L-Tubistor scaffolds showing E) the whole sample and F) a cut of the sample illustrating the luminal channel. EIS of the scaffold-based electrodes showing the G) Bode, Nyquist (inset) and H) phase plots. A 2-electrode configuration is used for the EIS measurements. The WE consists of a single point base Au electrode (2.5 mm × 2.5 mm) embedded in the PEDOT:PSS porous scaffold. A Pt mesh CE is placed at a fixed distance (≈4 mm) from the luminal scaffold, inside the plastic housing. I) Output (V_{GS} = 0 to 0.8 V, with a V_{GS} step of 0.1 V) and J) transfer curves from the L-Tubistor (measured at fixed V_{DS} = –0.8 V) and the corresponding transconductance curve.

to the increased dimensions/volume of the PEDOT:PSS scaffold, as well as to the presence of the lumen within the scaffold, likely improving the hydration of the scaffold and the electrolyte interfacing.

3. Establishment of the 3D Bioelectronic Human Intestine

We used a co-culture of intestinal epithelial cells (IECs) comprising Caco-2 cells and HT29-MTX cells (in a 3:1 ratio to mimic in vivo conditions), commonly found in in vitro models of the intestinal barrier.[17,45,46] Both cell lines are derived from human adenocarcinoma, however in culture they spontaneously differentiate toward mature enterocyte-like (Caco-2) and goblet-like cells (HT29-MTX) forming functional intestinal epithelial layers with a typical apical brush border and tight junctions. The presence of goblet cells in our culture system was considered critical for the formation of the mucus layer that lines the GI track, reinforcing intestinal barrier function.[11,45]

To evaluate our cell seeding strategy, at the end of the experiment, we disassembled the devices, carefully removed the embedded gold electrodes, extracted the scaffolds and fixed the cells within for optical characterization. Prior to imaging, we sectioned the scaffolds along the transverse and longitudinal directions to slices of ≈100 μm in thickness to enhance image quality. SEM revealed cell coverage of the electroactive scaffolds, exhibiting sufficient support of cell spreading and growth for 26 days in culture (**Figure 2**A). Typical intestinal biomarkers were used to evaluate the quality of the barrier formed, including the tight junction protein zonula occludens-1 (ZO-1) and mucin 2 (MUC2). Consistent expression of these molecules was observed, however, a closer look reveals formation of a discontinuous epithelial layer. This suggests that IECs infiltrated the bulk compartment of the scaffold, forming non-polarized "epithelial patches," rather than a uniform intestinal epithelial layer (Figure 2B–F). This is in line with our previous findings, where MDCKII (Madin–Darby Canine Kidney) cells formed epithelial tissue that lined scaffold walls, with no clear polarization.[44] We also observed that mucin was secreted toward the interior of these pore-pockets, lined by the "epithelial patches".

In vivo, the GI epithelium is supported by an underlying connective tissue layer, the lamina propria, which we posited might aid in generating stratified tissue organization. To reconstruct the lamina propria, we used human telomerase immortalized fibroblasts (TIF LifeAct), known for their ability to secrete growth factors and ECM proteins.[33,42,44] TIFs grown in the L-Tubistor for 26 days were shown to disperse throughout the scaffolds, infiltrating the bulk compartment and lining the walls of the pores (Figure 2G). We observed the characteristic elongated shape of fibroblasts, coating the surface of the material and forming typical fibrillar networks (Figure 2H–L), as expected. ECM protein secretion was confirmed by immunofluorescence staining for the expression of collagen I, laminin, and fibronectin. An extensive network of these ECM proteins was observed, co-localized with fibroblasts coating the surface of the material, representing an ideal lamina propria mimic (Figure S3, Supporting Information).

Cells growing on conducting scaffolds significantly alter the electrical properties of the material by impeding efficient ionic signal transduction,[33,42,44] in line with phenomena observed in 2D devices.[18,29] EIS was used to monitor the status of each 3D cell culture system throughout the culture duration by assessing the electrical response of L-Tubistors (Figure 2N,O). Given the more complex nature of the porous 3D CP scaffold, compared to 2D electrodes, we have attempted to understand how best to interpret EIS data with and without cells as detailed in Figure S4, Supporting Information. The resulting model allows us to monitor changes in the resistance and capacitance associated with cell infiltration into the bulk of the scaffold as well as cell growth and subsequent tissue formation. As expected, the impedance magnitude of IEC-cultured scaffolds increases at the mid to low frequency range (0.5–2 kHz), manifesting blocking of ion flow, a typical characteristic of barrier tissue forming cells. In contrast, we observed a consistently dramatic decrease in the overall impedance magnitude of TIF-cultured scaffolds and a shift in the phase toward slightly higher frequencies. These differences can be explained considering the different nature and properties of each tissue. Fibroblasts are adherent cells that need to stick to a surface to proliferate and grow rapidly, covering the available space with elongated fibrillar structures. As demonstrated by ECM protein staining (Figure S3, Supporting Information), scaffolds were fully infiltrated by TIFs and an extensive ECM protein network. This might affect the size and properties of the porous electrode, explaining the dramatic decrease in impedance magnitude observed. Another explanation suggests an enhancement in scaffold hydration or better distribution of charge species within the porous electrode due to the presence of ECM proteins.[47] As evidenced by the increased maximum in the phase spectrum, these layers of tissue act as a capacitive coating on the porous electrode, while they don't appear to significantly reduce ionic flux, but rather enhance the conductivity of the electrode. We did not observe this in our earlier work,[44] likely due to the optimized infiltration of cells, thanks to enhanced nutrient availability in the central lumen of the L-tubistor. IECs however, line the scaffolds with epithelial layers, with cells connected via a dynamic network of tight junctions that regulate the resistance of the barrier to ion flux. A mature, tight epithelial barrier on the WE thus acts both as a capacitive and resistive coating of the WE.[48]

Once we had ensured that the TIFs were suitable for a long-term experiment and formed a lamina propria, we designed a two-step process for the generation of a triple co-culture cell system with TIFs seeded on day 0, followed by IECs on day 4. This co-culture system was routinely maintained in static culture for three more weeks to allow for epithelial cells to differentiate toward a functional intestinal barrier. SEM and confocal microscopy (**Figure 3**A–F) allowed assessment of the distribution of cells in the pores of the scaffolds and tissue organization. In the presence of the lamina propria, the discontinuous layers from Figure 2B–F are not observed. Instead, IECs were seen to anchor on the fibroblast-layer, lining the luminal compartment of the scaffolds, differentiating toward a uniform continuous polarized intestinal epithelium, as illustrated in Figure 3G, showing polarized cells expressing TJs, with nuclei restricted to the basal side of the epithelium and a layer of mucin at the apical surface, toward the luminal hollow, as expected.

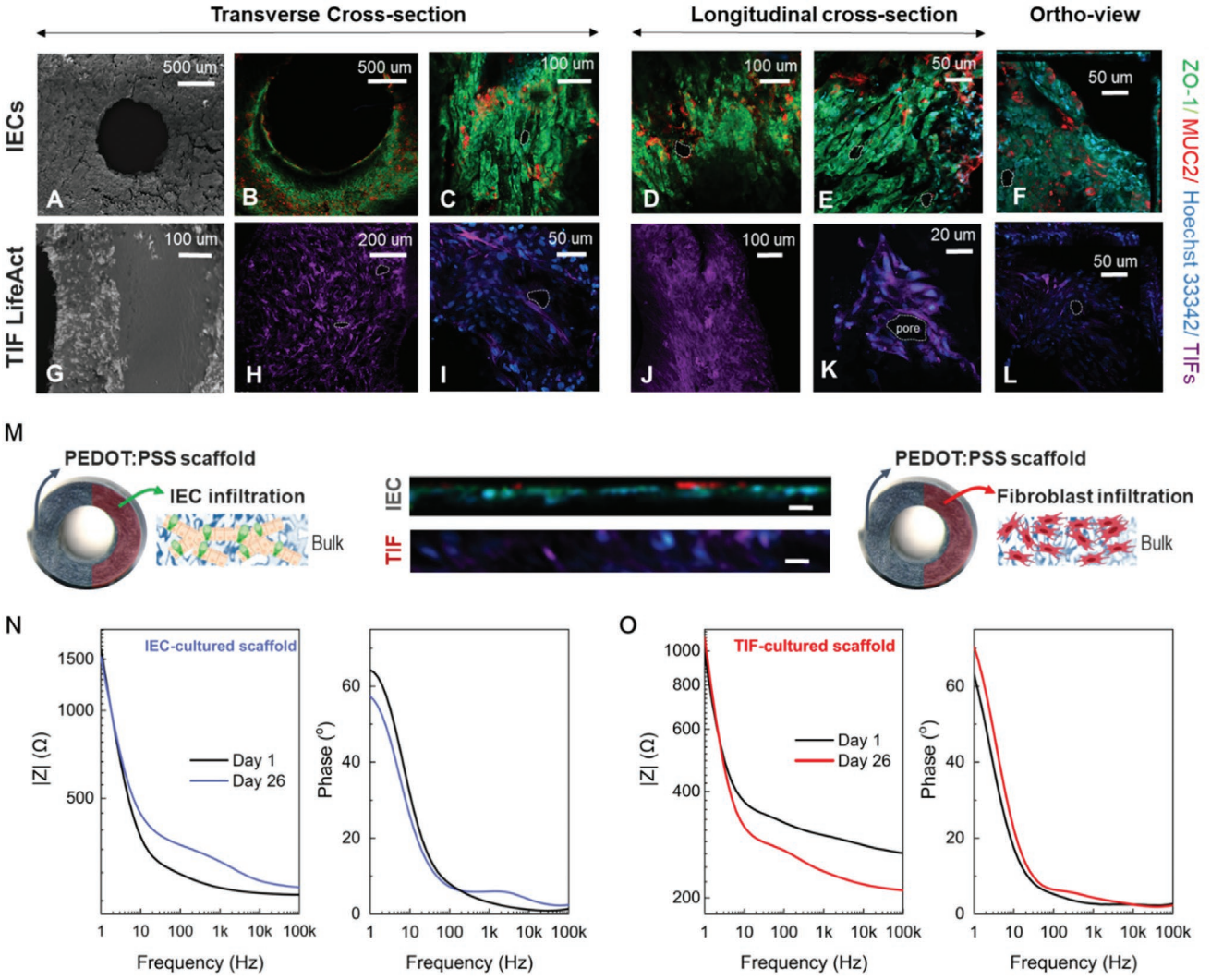

Figure 2. Establishment of the intestinal epithelium and lamina propria culture systems in L-Tubistors. SEM images of transverse sections of the electroactive scaffolds illustrating coverage of the porous network by A) co-culture of IECs (3:1 Caco-2/HT29-MTX cells) and G) TIF Life Act. B–F) Immunostained transverse and longitudinal sections of the IEC co-culture system, exhibiting consistent tight junction formation (ZO-1 in green) and mucus secretion (MUC2 in red), counterstained for nuclei (Hoechst 33 342 in blue). Patches of epithelial layers growing on individual porous domains can be observed. H,I) Confocal images of TIF cells (tagged with RFP but shown in purple here), counterstained for nuclei (Hoechst 33 342 in blue) demonstrating cell infiltration and formation of the characteristic fibrillar networks. Images (F) and (L) are orthogonal views (ortho-view) of z-stack confocal images (Movies S1 and S2, Supporting Information), showing the *x*/*y* (center), *x*/*z* (top), and *y*/*z* (right) views of scaffold sections of each culture mode. White dashed lines are indicative of pores, lined by different types of cells. M) Schematic illustration of cell infiltration through the bulk compartment of the scaffolds hosting fibroblasts (right) and IECs (left). Magnified *x*/*z* ortho-views (middle of M) of panels F and L showing cell infiltration and organization in the porous network of PEDOT:PSS scaffolds for each culture system. Black gaps in some of the images are due to the difficulty to acquire all focal planes in one 2D image because of the complexity of the 3D samples. EIS characteristics showing impedance magnitude (Bode) and phase curves of the N) IEC-cultured and O) TIF-cultured scaffolds, respectively. The IEC-cultured scaffold exhibits a distinct increase in the impedance magnitude at the mid/low frequencies range (0.5–2 kHz) after 26 days of cell culture. Phase Bode spectra also reveals the presence of a characteristic time constant at ≈2 kHz which can be attributed to the formation of an extensive barrier-like tissue within the scaffold. In contrast, in the case of the TIF culture a dramatic decrease in the overall impedance magnitude can be observed between day 1 (black solid line) up to day 26 (red solid line).

Turning now to electrical monitoring of the tri-culture model, we looked first at the complex impedance during the initial phase of the experiment and the behavior of the device before and after each seeding stage to extract information about cell adhesion and growth. We compared impedance changes resulting from overnight growth of cells after each seeding stage (Figure 3H); before seeding fibroblasts (day 0), after overnight cultivation of TIFs (day 1), before seeding IECs (day 4) and after overnight incubation with IECs (day 5) and show the relative change in the capacitance ($\Delta C/C_o$) and resistance ($\Delta R/R_o$) at each stage (Figure 3I). Overnight cultivation of fibroblasts results in a marked change in the capacitance and a less prominent change in resistance, as before (Figure 2N). Upon injecting the IECs into the fibroblast-seeded scaffold, the capacitance appears to be marginally affected, while the resistance undergoes a significant increase. Changes in the resistance may be partially affected by the switching of

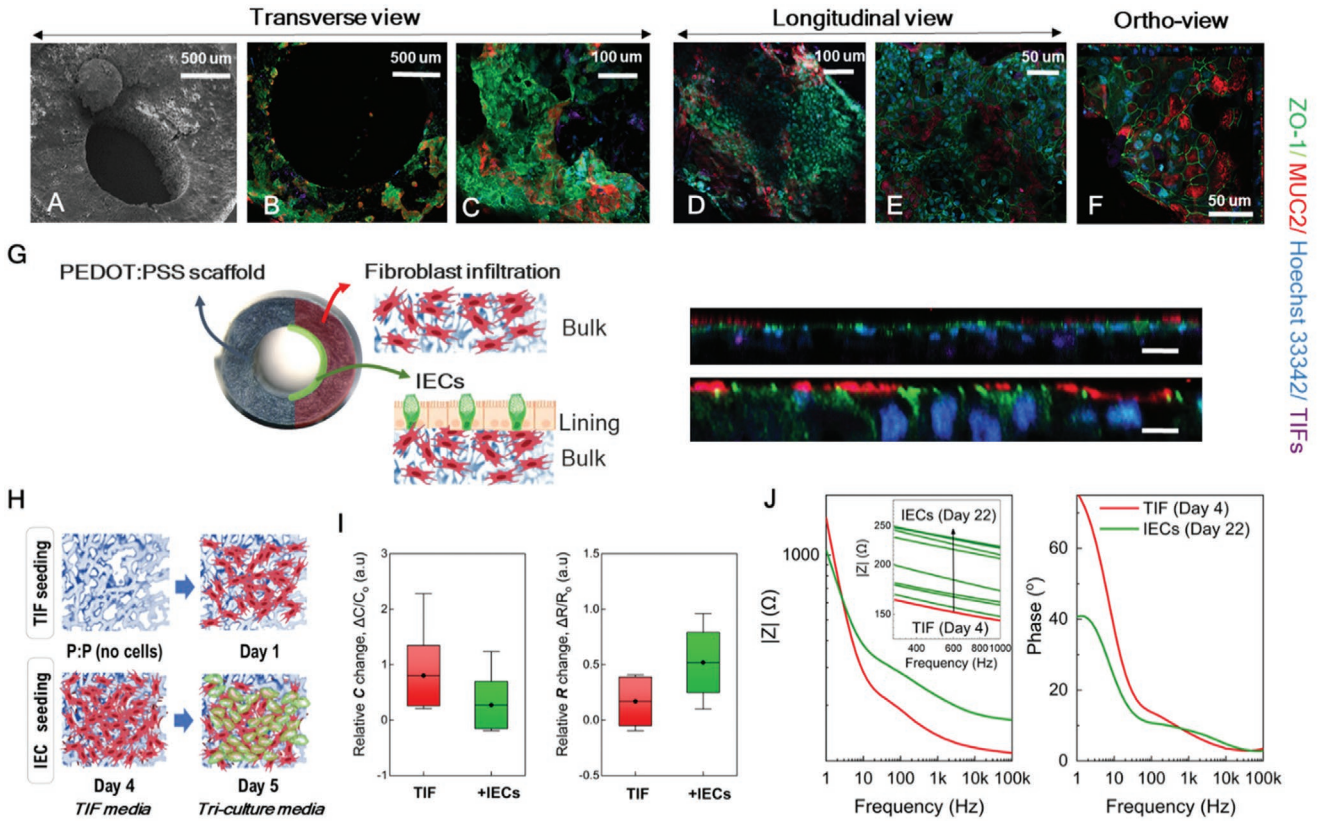

Figure 3. The 3D bioelectronic human intestine hosted in L-Tubistors. A) SEM image illustrating cell coverage of the scaffolds by the tri-culture model. B–F) Immunostained transverse, longitudinal, and orthogonal sections of the 3D bioelectronic intestinal model, demonstrating enteric cells forming a continuous epithelial layer on the lumen lining supported by the lamina propria layer in the bulk compartment of the L-Tubistor scaffolds. Consistent expression of tight junctions (ZO-1 in green) and mucin secretion (MUC2 in red) can be observed, nuclei are shown in blue (Hoechst 33 342). Image F) is an orthogonal view obtained by z-stacked confocal images, showing the *x*/*y* (center), *x*/*z* (top), and *y*/*z* (right) views of the sample. G) A schematic illustration of the bioelectronic platform hosting the human intestine model (left). Magnified *x*/*z* orthogonal views (ortho-views, right) of the samples obtained by z-stacked confocal images (Movies S3 and S4, Supporting Information), illustrating the organization of fibroblasts and IECs in the scaffold microenvironment according to the seeding strategy, with IECs anchoring on the lamina propria to form the intestinal tissue with proper polarization characteristics and a typical brush boarder toward the lumen lining of the scaffolds. H–J) Impedance study of the adhesion and growth of the two types of cells on the luminal electrodes. H) Schematic illustration of the two stages of cell seeding and proliferation inside the porous electrode. The first stage corresponds to the seeding of TIFs in the bare scaffold (day 0) and the second stage corresponds to the seeding of IECs on the TIF-cultured scaffold (day 4). In both cases, the impedance response was monitored after overnight cell cultivation in the respective growth-medium. The *R*, *C* parameters were extracted from the impedance spectra as shown in the Nyquist plots of Figure S5, Supporting Information. Box plots showing the I) relative change in the capacitance ($\Delta C/C_o$) and resistance ($\Delta R/R_o$) of the porous electrodes ($n = 5$) after each stage of seeding. J) Representative Bode impedance magnitude and phase plots, showing the initial (red line, day 4 of TIF culture) and the final response (green line, day 22 of IEC culture) of the cultured luminal electrodes. Inset in Bode plot shows the evolution of the complex impedance during the tissue formation, from day 4 of TIF culture to day 22 of IEC culture (overall day 26 for the tri-culture system).

culture medium from TIF-medium to tri-culture medium. However, this is expected to be negligible as the media have similar pH and ionic composition, and as shown in Figure S6, Supporting Information, the overall device performance and stability was not affected by cell culture media, nor did routine changes of media compromise the electrical readouts. The observed stability of our device is in agreement with previous studies on PEDOT:PSS-coated gold electrodes, showing no significant performance alterations after 4 months in cell culture media.[49] EIS monitoring of the 26-day tri-culture experiment is shown in Figure 3J. We observed a significant increase of the overall magnitude of the impedance during the proliferation of intestinal cells and the maturation of the epithelial barrier. From day 1 of IEC culture, the cells modulate the electrode characteristics and as the epithelial layer is formed, the magnitude of the complex impedance shifts toward higher values, until it reaches a plateau at the last stages of the culture, corresponding to a polarized, mature epithelium with a typical brush border and mucin layer at the apical side (as cross-validated optically). The increase of the impedance magnitude in the tri-culture intestinal model is not as dramatic as in the IEC-cultured scaffold, (Figure 2) likely due to the formation of a single continuous epithelial layer on top of the stroma, rather than multiple layers of epithelium infiltrating the scaffold bulk. The phase data in Figure 3J demonstrate a considerable decrease of the phase maximum at low frequencies and the presence of a typical time constant in the mid-frequency range of the spectrum, more pronounced here compared to the IEC- only cultured L-Tubistor.

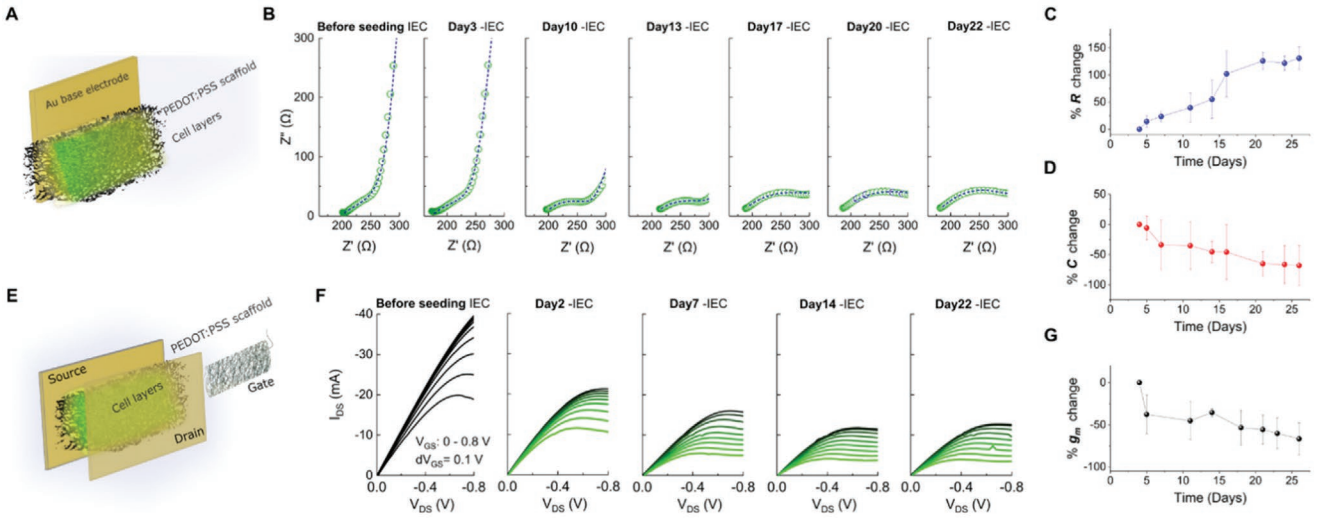

Figure 4. Bimodal (electrode/transistor) electrical monitoring of the 3D intestinal model during cell growth. A) Schematic showing the electrode mode of operation using the cell cultured PEDOT:PSS scaffold. B) Evolution of the Nyquist plots of a representative sample during 22 days of IEC culture. Dashed blue line corresponds to a fit of the experimental data using the equivalent circuit shown in (A) used for the calculation of the % relative change versus time in the C) resistance ($\Delta R/R_o$) and D) capacitance ($\Delta C/C_o$) of the porous electrodes ($n = 4$). E) Schematic showing the transistor mode of operation with the cultured PEDOT:PSS scaffold as the channel between two Au source-drain electrodes and a Pt mesh gate electrode in close proximity. F) Evolution of the output IV characteristics ($V_{GS} = 0$ to 0.8 V, with a V_{GS} step of 0.1 V) of a representative sample at distinct time points during 22 days of IECs culture. G) % relative change versus time in the maximum transconductance ($\Delta g_m/g_{mo}$) of the transistor as calculated by $\Delta I_{DS}/\Delta V_{GS}$ ($n = 4$). Initial curve (before seeding IEC) in the dataset corresponds to the TIF-cultured electrode after 4 days of incubation and represents the baseline of our measurements.

Bimodal operation of our device allows cross-validation of findings associated with changes in the electronic properties of the PEDOT:PSS scaffold at different time points, providing complementary information (configurations are illustrated in **Figures 4**A,E). Electrode operation (EIS mode) allows for extraction of large amounts of quantitative information through careful use of the equivalent circuit (Figure S4, Supporting Information). In contrast, transistor operation provides a quick reading that is more qualitative in nature, as the large surface area prohibits frequency dependent measurements.

EIS measurements of the magnitude of changes caused by the evolution of the tri-culture system toward an intestinal barrier over time are shown in Figure 4B. Before seeding IECs, the impedance curve exhibits a slightly bent, branched behavior at high frequencies and a tilted line at lower frequencies. Both branches deviate from ideal capacitive conditions, validating the use of constant phase elements (CPEs) in our model. After IEC seeding, the Nyquist plots at high frequencies resemble a semicircle pattern, attributed to the presence of the IECs and the formation of a tissue layer. We observe a temporal increase in the projected semicircle, suggesting a continuous increase in the resistance at the luminal/pore interface, reaching a plateau after week 2 of IEC culture. This response is consistent with the gradual covering of the electrode followed by epithelial tissue differentiation. The evolution of the relative resistance and capacitance (i.e., the change vs the initial value, $\Delta R/R_o$ and $\Delta C/C_o$, respectively) over time can be seen in Figure 4C,D, respectively. As expected, the addition of cells introduces barriers to ion transport, resulting in an overall increase in the resistance of the system over time (Figure 4C). Likewise, the bulk capacitance (Figure 4D) of the system decreases with time. A peak $\Delta R/R_o$ was observed after 2 weeks of IEC culture while $\Delta C/C_o$ revealed a gradual decrease (with an acute initial drop) over time. This behavior is likely attributable to the decrease of the available surface area (hence the volumetric capacitance of the scaffold) due to the presence of cells at the luminal interface and the formation of tight junctions at this stage of tissue development.

Transistor operation (Figure 4E), illustrated similar behavior in the evolution of the output characteristics (Figure 4F). The gradual decrease in the maximum saturation current over time (I_{DS} at $V_{GS} = 0$ V, $V_{DS} = -0.8$ V), can be attributed to a decrease in the conductance of PEDOT:PSS, as a result of the cell coverage, or to a potential drop at the channel electrolyte interface affecting the gating efficiency. Transconductance reflects the magnitude of the amplification of the transistor and hence its sensitivity in transducing biological events (related to the cell growth and coverage in this case), and is proportional to the volumetric capacitance of the PEDOT:PSS channel,[50] which is in turn affected (decreased) by the presence of the cell layer (Figure 4G). A substantial initial drop in the relative g_m over time is observed, similarly to Figure 4D, attributed to the initial phase of cell growth, consistent with previous observations.[44]

4. Conclusion

OoC platforms have seen enormous progress in recent years, however the present hurdle is moving away from 2D cultures to more accurately replicating native 3D tissues. This presents a significant challenge to the integration of real-time, sensing capabilities. Here, we have combined tissue engineering with bioelectronics, to develop the L-Tubistor, a 3D bioelectronic

model of the human intestine. This work represents the first instance of a 3D human intestinal tissue with seamlessly integrated sensing components incorporated into the heart of the tissue, that allow for continuous monitoring of cell status and activity for 1 month. We demonstrate bimodal operation of the L-Tubistor, using the device both as an electrode for EIS monitoring, and as a transistor. Flexibility in the device configuration, along with the complementarity of the two modes of operation, allows for rapid, straightforward and qualitative evaluation of our tissue model combined with more quantitative EIS measurements. Our seeding strategy, first establishing a connective tissue, representative of the lamina propria in the bulk compartment of the porous electrode, followed by subsequent layering of the intestinal epithelium on the lumen lining, resulted in a 3D intestinal culture system that reconstitutes both structural and functional properties of the native tissue. The integrated electronics allowed for close and continuous monitoring of the establishment of both tissue types throughout the almost 4-week experiment, as well as for prompt decisions about the course of the experiment to be made early on, in a non-invasive, non-destructive manner, saving valuable research time and effort. Electrical signatures from different cell and tissue types emerge clearly from our work. During both stages of cell seeding, we were able to confirm the presence, adhesion, and growth of cells in the porous electrode by assessing impedance characteristics and extracting information about the contribution of cell activity to the capacitance and resistance of the system. It was expected that different tissue types would result in different changes in the impedance spectra and transistor outputs. Indeed, IECs, as barrier forming cells, inhibited ion flow and thus increased the resistance of the devices. In combination with fibroblasts, the increase is less prominent, presumably due to the formation of a single tissue epithelium, rather than multiple layers of epithelia. The decrease of the overall impedance magnitude observed in the TIF-cultured L-Tubistor is a very useful marker for growth and proliferation of this cell type. Ongoing experiments are focused on unraveling the interaction between fibroblasts and the porous electrode material.

These observations highlight the unparalleled capabilities of our bioelectronic system to dynamically monitor complex cellular systems and reveal information about different biological events, providing better control for engineering tissues. Our focus is now shifted to further advancing the model, both from the biological and engineering standpoint. Future work will focus on integration of our 3D bioelectronic human intestine into a multi-OoC platform for disease modeling and drug development. The resulting platform will be used to assess the effect of agents such as pathogens, or novel probiotics on intestinal integrity.

5. Experimental Section

Device Fabrication: Scaffolds were prepared inside the tubing inserts from an aqueous dispersion of PEDOT:PSS (Clevios PH-1000, Heraeus) at a concentration of 1.25 wt%. To further enhance the conductivity of the PEDOT:PSS scaffolds dodecylbenzenesulfonic acid (DBSA, Sigma Aldrich) (0.5%) was added to the PEDOT:PSS pristine solution. To enhance the mechanical properties and the stability of the scaffolds, (3-glycidoxypropyl)-trimethoxysilane (GOPS, Sigma Aldrich) was added as a crosslinker (3%wt). For the fabrication of the luminal scaffold a 16G stainless steel needle was inserted inside the tube as seen in Figure S1, Supporting Information. To maintain the needle at the center of the tube, two sealing caps were used at both ends. This also helped to adjust more accurately the volume of the injected solution inside the tube. The samples were then placed in a freeze-dryer (Virtis AdVantage 2.0 BenchTop from SP Scientific) and they were frozen from 5 to –40 °C at a controlled cooling rate, after which point the ice phase was sublimed from the scaffolds. The needle was then removed and the samples were baked at 70 °C for 4 h. Prior to cell experiments, the scaffolds were rinsed with deionized (DI) water multiple times and they were then kept in DI water for 24 h.

For the fabrication of the well-plate inserts, polypropylene tee-shaped (Cole Parmer) tubes were used to host the scaffold structures. The tubing support had an inner diameter of 4 mm and a length of 15 mm. The electrical terminals were made of flexible Au (150 nm) /Kapton foils and they were placed inside the tube using the top opening part of the tube. A temporary separator was used to avoid contact between the two (S-D) electrodes. Cytocompatible glue was used to seal the top opening part. For the gate/CE a Pt mesh (20 mm × 20 mm) was used. The inserts were adapted on the lid.

Cell Culture Maintenance: TIFs labeled with red fluorescent protein (RFP–TIF LifeAct, a gift from Ellen Van Obberghen-Schilling, Institut de Biologie de Valrose), Caco-2 cells (ECACC), and HT29-MTX cells (ECACC) were routinely maintained before all experiments. Caco-2 cells (P50-58) were cultured in Advanced DMEM (Gibco, Life technologies), supplemented with 10% fetal bovine serum (FBS, Sigma Aldrich), 1% M Glutamine (Glutamax-1; Invitrogen) 1% penicillin–streptomycin (10 000 U mL^{-1}, Gibco, Life technologies) and 0.1% Gentamicin (Sigma Aldrich) while HT29-MTX (P54-58) cells were cultured in Advanced DMEM (Gibco, Life technologies), supplemented with 10% FBS (Sigma Aldrich), and 1% penicillin–streptomycin (10 000 U mL^{-1}, Gibco, Life technologies). TIF LifeAct (P9-12) were cultured in Advanced DMEM (Gibco, Life technologies) supplemented with 20% FBS (Sigma Aldrich), 1% Glutamine (Gibco, Life technologies), 2% HEPES (Gibco, Life technologies), 0.5% penicillin–streptomycin (10 000 U mL^{-1}, Gibco, Life technologies), and 0.1% Gentamicin (Sigma Aldrich). All cells were cultured in T-75 flasks, maintained at 37 °C, 5% CO_2 humidified atmosphere and harvested with 0.25–0.5% trypsin-prior to seeding or passaging.

Seeding Process: Cells were routinely maintained as described above until the day of the experiments. On the day of the experiment (day 0), the L-Tubistor scaffolds were sterilized with 70% ethanol and thoroughly rinsed with sterile DI water and PBS, followed by immersion in complete growth medium for 2 h, to allow for protein adhesion, and then washed with fresh medium. The scaffolds were seeded either with IEC or TIF cell suspension at a density of 2×10^6 cells mL^{-1} using a syringe, incubated for 2 h to allow for cell adhesion and attachment, before immersing the devices in fresh complete growth medium. This 3D cell culture system was maintained for 26 days, with media being changed three times per week. To test whether fibroblasts secrete ECM proteins, scaffold discs/slices (1 cm diameter, 500 µm thickness) with the same morphological properties as the L-Tubistor scaffolds were used, following the same sterilization and seeding method. This TIF-culture was routinely maintained for 5 days to allow for infiltration of the scaffold slices and ECM network formation. For the generation of the tri-culture model a 2-stage seeding protocol was followed. On day 0 of the experiment, L-Tubistors were treated as before for sterilization and preparation for seeding and then a TIF cell suspension of 2×10^6 cells mL^{-1} was injected in the devices using a syringe, followed by 2-hour incubation before immersing the devices in TIF culture medium. After this first stage of seeding, the culture was maintained for 4 days to allow TIFs to proliferate, line the pores of the bulk of the scaffold and secrete ECM. At the second stage, these pre-seeded with TIFs L-Tubistors were seeded with a co-culture of Caco-2 and HT29-MTX cells (3:1 ratio) at a density of 2×10^6 cells mL^{-1} using a syringe. Again the cells were incubated for 2 h to allow for cell adhesion and attachment, before immersing the devices in fresh complete growth medium, for which the composition

was adjusted to accommodate the needs of all cell lines (i.e., tri-culture medium).

Electrical Characterization: The impedance measurements were carried out using a potentiostat (Autolab, Metrohm) equipped with a frequency response analysis module. A 2-electrode electrochemical cell configuration was used with the CP scaffold/Au base electrode acting as the WE and a Pt mesh (20 mm × 20 mm) as the CE. The potentiostat cables were connected as CE+RE and the WE+WS in order to create the 2-electrode electrochemical cell. The distance between the two electrodes was set at ≈4 mm. The applied AC voltage was 0.01 V and measurements were carried out at 0 V DC potential versus open circuit potential. The frequency was varied from 100 kHz to 100 mHz and recording 10 points per decade. Analysis was performed using EC-Lab (Bio-Logic) software using the model described in Figure S4, Supporting Information. For the calculation of the pseudo-capacitance associated with a CPE in the R/Q branch, the following formula was used:[51]

$$C = \frac{(RQ)^{\frac{1}{a}}}{R} \quad (1)$$

where Q is the magnitude of the CPE and a is exponent of the CPE.

Transistor characteristics were taken using a Keithley 2612B source meter and customized LabVIEW software. The flexible Au electrodes were assigned as the source and drain electrodes and the Pt mesh as the gate electrode. All the electrical measurements were acquired in the corresponding cell culture media, unless otherwise stated.

Immunofluorescence Staining: TIFs, Caco-2, HT29-MTX cells, and their co-cultures were fixed in 4% paraformaldehyde (PFA, ThermoFischer Scientific) for 20 min, at room temperature. All samples were thoroughly washed with PBS, permeabilized in 0.1% Triton ×-100 for 15 min and then blocked for nonspecific binding with 1% BSA and 0.1% Tween-20 for 1 h at room temperature. To label the samples for tight junction protein zonula occludens-1 (ZO-1), mucin protein (MUC2), ECM proteins and nuclei, the following primary and secondary antibodies were used: Rb polyclonal anti-ZO-1, (ThermoFisher Scientific), Ms monoclonal anti-MUC2, (abcam), Rabbit Anti-Laminin 1+2 (abcam), Mouse Anti-Fibronectin (abcam), Mouse Anti-Collagen I (abcam), Bisbenzamide H (Hoechst 33342, abcam), Goat-anti-rabbit Alexa Fluor 488 (abcam), Goat-anti-mouse Alexa Fluor 647 (abcam). Samples were sectioned along the longitudinal and transverse axes using scalpels. Fluorescence images of scaffold sections were obtained using an epifluorescence/confocal microscope (Axio Observer Z1 LSM 800, Zeiss).

Scanning Electron Microscopy: Scaffold microstructure with and without cells was characterized using SEM (Leo Variable pressure SEM, ZEIS GmbH). In particular, SEM was used to visualize the macroporous network of the scaffolds without cells and then evaluate the invasion of cells in the pores as well as the cell coverage in each case. Briefly, cells in the scaffold were fixed in 4% PFA for 20 min at room temperature, washed thoroughly with PBS, dehydrated in a graded ethanol series and then in hexamethyldisilazane solution (Sigma Aldrich) until complete dehydration. Finally, the samples were mounted on conductive adhesion tape and analyzed at 1 kV power.

X-ray Microcomputed Tomography: XμCT measurements were conducted using a SkyScan 1172 scanner (Bruker, Antwerp, Belgium) to investigate the microstructure of PEDOT:PSS hollow tubular scaffolds. The XμCT measurements were performed in a cone-beam configuration without using a filter. The sample was rotated at an angular rotation step of 0.06° over 360° and 2D projection images of the sample were recorded at each rotation step at an isotropic voxel resolution of 2.3 μm and an exposure time of 1600 ms. The 2D projection images were then reconstructed using NRecon software (Bruker, Version: 1.7.4.2) to obtain cross-section images of the samples. The reconstructed images were then visualized and aligned using DataViewer software (Bruker, Version: 1.5.6.2) to obtain 2D cross-sections of the sample at different positions, (i.e., top and bottom of the sample). CTAn software (Bruker, Version: 1.18.4.0) was used to binarize the reconstructed images and calculate the porosity of the sample. CTvox software (Bruker, Version: 3.3.0) was also used to create a 3D model and a video of the sample using the reconstructed images.

Supporting Information

Supporting Information is available from the Wiley Online Library or from the author.

Acknowledgements

The authors wish to acknowledge funding from the European Research Council (ERC) under the European Union's Horizon 2020 research and innovation program (grant agreement No. 723951) (C.-M.M., C.P., A.M.W., and R.M.O.). Johnson Matthey and the U.K. Engineering and Physical Sciences Research Council (EPSRC) are also acknowledged for the funding of the Ph.D. project of M.A.

Conflict of Interest

The authors declare no conflict of interest.

Author Contributions

C.-M.M. and C.P. contributed equally to this work. C.-M.M. and C.P. conceived, executed, and analyzed results of experiments. A.M.W. aided with cell culture maintenance. M.A. and J.A.Z. did the XμCT experiments and their subsequent image analysis. R.M.O. conceived and directed research on the paper. The manuscript was written and edited by C.-M.M., C.P., and R.M.O.

Keywords

Bioelectronics, impedance, intestine, organic electrochemical transistors, organ-on-chip

Received: September 26, 2020
Revised: November 26, 2020
Published online:

[1] K. R. Groschwitz, S. P. Hogan, *J. Allergy Clin. Immunol.* **2009**, *124*, 3.
[2] L. Thoo, M. Noti, P. Krebs, *Cell Death Dis.* **2019**, *10*, 849.
[3] J. F. Cryan, K. J. O'Riordan, K. Sandhu, V. Peterson, T. G. Dinan, *Lancet Neurol.* **2019**, *19*, 179.
[4] S. C. Pearce, H. G. Coia, J. P. Karl, I. G. Pantoja-Feliciano, N. C. Zachos, K. Racicot, *Front. Plant Physiol.* **2018**, *9*, 01584.
[5] J. A. Gilbert, R. A. Quinn, J. Debelius, Z. Z. Xu, J. Morton, N. Garg, J. K. Jansson, P. C. Dorrestein, R. Knight, *Nature* **2016**, *535*, 94.
[6] A. Ziegler, L. Gonzalez, A. Blikslager, *Cell. Mol. Gastroenterol. Hepatol.* **2016**, *2*, 716.
[7] J. A. Jiminez, T. C. Uwiera, G. D. Inglis, R. R. E. Uwiera, *Gut Pathog.* **2015**, *7*, 29.
[8] I. Kola, J. Landis, *Nat. Rev. Drug Discovery* **2004**, *3*, 711.
[9] J. Costa, A. Ahluwalia, *Front. Bioeng. Biotechnol.* **2019**, *7*, 00144.
[10] A. Bein, W. Shin, S. Jalili-Firoozinezhad, M. H. Park, A. Sontheimer-Phelps, A. Tovaglieri, A. Chalkiadaki, H. J. Kim, D. E. Ingber, *Cell. Mol. Gastroenterol. Hepatol.* **2018**, *5*, 659.

[11] T. Lea, in *The Impact of Food Bioactives on Health: In Vitro and Ex Vivo Models*, (Eds: K. Verhoeckx, P. Cotter, I. López-Expósito, C. Kleiveland, T. Lea, A. Mackie, T. Requena, D. Swiatecka, H. Wichers), Springer, Cham, Switzerland **2015**, 95.
[12] S. N. Bhatia, D. E. Ingber, *Nat. Biotechnol.* **2014**, *32*, 760.
[13] E. Knight, S. Przyborski, *J. Anat.* **2015**, *227*, 746.
[14] A. Roth, T. Singer, *Adv. Drug Delivery Rev.* **2014**, *69–70*, 179.
[15] E. R. Shamir, A. J. Ewald, *Nat. Rev. Mol. Cell Biol.* **2014**, *15*, 647.
[16] M. Kasendra, A. Tovaglieri, A. Sontheimer-Phelps, S. Jalili-Firoozinezhad, A. Bein, A. Chalkiadaki, W. Scholl, C. Zhang, H. Rickner, C. A. Richmond, H. Li, D. T. Breault, D. E. Ingber, *Sci. Rep.* **2018**, *8*, 2871.
[17] Y. Chen, Y. Lin, K. M. Davis, Q. Wang, J. Rnjak-Kovacina, C. Li, R. R. Isberg, C. A. Kumamoto, J. Mecsas, D. L. Kaplan, *Sci. Rep.* **2015**, *5*, 13708.
[18] M. W. van der Helm, O. Y. F. Henry, A. Bein, T. Hamkins-Indik, M. J. Cronce, W. D. Leineweber, M. Odijk, A. D. van der Meer, J. C. T. Eijkel, D. E. Ingber, A. van den Berg, L. I. Segerink, *Lab Chip* **2019**, *19*, 452.
[19] K. Ronaldson-Bouchard, G. Vunjak-Novakovic, *Cell Stem Cell* **2018**, *22*, 310.
[20] A. Sin, K. C. Chin, M. F. Jamil, Y. Kostov, G. Rao, M. L. Shuler, *Biotechnol. Prog.* **2008**, *20*, 338.
[21] A. Herland, B. M. Maoz, D. Das, M. R. Somayaji, R. Prantil-Baun, R. Novak, M. Cronce, T. Huffstater, S. S. F. Jeanty, M. Ingram, A. Chalkiadaki, D. Benson Chou, S. Marquez, A. Delahanty, S. Jalili-Firoozinezhad, Y. Milton, A. Sontheimer-Phelps, B. Swenor, O. Levy, K. K. Parker, A. Przekwas, D. E. Ingber, *Nat. Biomed. Eng.* **2020**, *4*, 421.
[22] N. Franzen, W. H. van Harten, V. P. Retèl, P. Loskill, J. van den Eijnden-van Raaij, M. IJzerman, *Drug Discovery Today* **2019**, *24*, 1720.
[23] J. A. Terrell, C. G. Jones, G. K. M. Kabandana, C. Chen, *J. Mater. Chem. B* **2020**, *8*, 6667.
[24] B. Zhang, A. Korolj, B. F. L. Lai, M. Radisic, *Nat. Rev. Mater.* **2018**, *3*, 257.
[25] R. Novak, M. Ingram, S. Marquez, D. Das, A. Delahanty, A. Herland, B. M. Maoz, S. S. F. Jeanty, M. R. Somayaji, M. Burt, E. Calamari, A. Chalkiadaki, A. Cho, Y. Choe, D. B. Chou, M. Cronce, S. Dauth, T. Divic, J. Fernandez-Alcon, T. Ferrante, J. Ferrier, E. A. FitzGerald, R. Fleming, S. Jalili-Firoozinezhad, T. Grevesse, J. A. Goss, T. Hamkins-Indik, O. Henry, C. Hinojosa, T. Huffstater, et al., *Nat. Biomed. Eng.* **2020**, *4*, 407.
[26] T. T. Roh, Y. Chen, H. T. Paul, C. Guo, D. L. Kaplan, *Biomaterials* **2019**, *225*, 119517.
[27] M. Trapecar, C. Communal, J. Velazquez, C. A. Maass, Y. J. Huang, K. Schneider, C. W. Wright, V. Butty, G. Eng, O. Yilmaz, D. Trumper, L. G. Griffith, *Cell Syst.* **2020**, *10*, 223.
[28] S. E. De León, A. Pupovac, S. L. McArthur, *Biotechnol. Bioeng.* **2020**, *117*, 1230.
[29] V. F. Curto, B. Marchiori, A. Hama, A.-M. Pappa, M. P. Ferro, M. Braendlein, J. Rivnay, M. Fiocchi, G. G. Malliaras, M. Ramuz, R. M. Owens, *Microsyst. Nanoeng.* **2017**, *3*, 17028.
[30] J. Rivnay, S. Inal, A. Salleo, R. M. Owens, M. Berggren, G. G. Malliaras, *Nat. Rev. Mater.* **2018**, *3*, 17086.
[31] S. A. Tria, M. Ramuz, M. Huerta, P. Leleux, J. Rivnay, L. H. Jimison, A. Hama, G. G. Malliaras, R. M. Owens, *Adv. Healthcare Mater.* **2014**, *3*, 1053.
[32] K. Benson, S. Cramer, H.-J. Galla, *Fluids Barriers CNS* **2013**, *10*, 5.
[33] S. Inal, A. Hama, M. Ferro, C. Pitsalidis, J. Oziat, D. Iandolo, A.-M. Pappa, M. Hadida, M. Huerta, D. Marchat, P. Mailley, R. M. Owens, *Adv. Biosyst.* **2017**, *1*, 1700052.
[34] A. Kalmykov, C. Huang, J. Bliley, D. Shiwarski, J. Tashman, A. Abdullah, S. K. Rastogi, S. Shukla, E. Mataev, A. W. Feinberg, K. J. Hsia, T. Cohen-Karni, *Sci. Adv.* **2019**, *5*, eaax0729.
[35] J. Pas, C. Pitsalidis, D. A. Koutsouras, P. P. Quilichini, F. Santoro, B. Cui, L. Gallais, R. P. O'Connor, G. G. Malliaras, R. M. Owens, *Adv. Biosyst.* **2017**, *1700164*, 1700164.
[36] V. F. Curto, M. P. Ferro, F. Mariani, E. Scavetta, R. M. Owens, *Lab Chip* **2018**, *18*, 933.
[37] H. G. Jahnke, A. Mewes, F. D. Zitzmann, S. Schmidt, R. Azendorf, A. A. Robitzki, *Sci. Rep.* **2019**, *9*, 13875.
[38] F. D. Zitzmann, H. G. Jahnke, F. Nitschke, A. G. Beck-Sickinger, B. Abel, D. Belder, A. A. Robitzki, *Lab Chip* **2017**, *17*, 4294.
[39] A. G. Guex, J. L. Puetzer, A. Armgarth, E. Littmann, E. Stavrinidou, E. P. Giannelis, G. G. Malliaras, M. M. Stevens, *Acta Biomater.* **2017**, *62*, 91.
[40] A. M. D. Wan, S. Inal, T. Williams, K. Wang, P. Leleux, L. Estevez, E. P. Giannelis, C. Fischbach, G. G. Malliaras, D. Gourdon, *J. Mater. Chem. B* **2015**, *3*, 5040.
[41] D. Iandolo, F. A. Pennacchio, V. Mollo, D. Rossi, D. Dannhauser, B. Cui, R. M. Owens, F. Santoro, *Adv. Biosyst.* **2018**, *3*, 1800103.
[42] A. K. Jayaram, C. Pitsalidis, E. Tan, C.-M. Moysidou, M. F. L. De Volder, J.-S. Kim, R. M. Owens, *Front. Chem.* **2019**, *7*, 00363.
[43] I. Del Agua, S. Marina, C. Pitsalidis, D. Mantione, M. Ferro, D. Iandolo, A. Sanchez-Sanchez, G. G. Malliaras, R. M. Owens, D. Mecerreyes, *ACS Omega* **2018**, *3*, 7424.
[44] C. Pitsalidis, M. P. Ferro, D. Iandolo, L. Tzounis, S. Inal, R. M. Owens, *Sci. Adv.* **2018**, *4*, eaat4253.
[45] R. H. Dosh, A. Essa, N. Jordan-Mahy, C. Sammon, C. L. Le Maitre, *Acta Biomater.* **2017**, *62*, 128.
[46] I. Lozoya-Agullo, F. Araújo, I. González-Álvarez, M. Merino-Sanjuán, M. González-Álvarez, M. Bermejo, B. Sarmento, *Mol. Pharmaceutics* **2017**, *14*, 1264.
[47] C. Frantz, K. M. Stewart, V. M. Weaver, *J. Cell Sci.* **2010**, *123*, 4195.
[48] J. A. Stolwijk, K. Matrougui, C. W. Renken, M. Trebak, *Pfluegers Arch.* **2015**, *467*, 2193.
[49] G. Dijk, A. L. Rutz, G. G. Malliaras, *Adv. Mater. Technol.* **2020**, *5*, 1900662.
[50] J. Rivnay, P. Leleux, M. Ferro, M. Sessolo, A. Williamson, D. A. Koutsouras, D. Khodagholy, M. Ramuz, X. Strakosas, R. M. Owens, C. Benar, J. M. Badier, C. Bernard, G. G. Malliaras, *Sci. Adv.* **2015**, *1*, e1400251.
[51] C. H. Hsu, F. Mansfeld, *CORROSION* **2001**, *57*, 747.